

Mach number influence on low-pressure turbine flutter

Original article

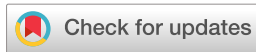
Article history:

Submission date: 1 December 2023

Acceptance date: 20 January 2024

Publication date: 11 April 2024

This is the updated version of a paper originally presented at the Global Power and Propulsion Technical Conference, GPPS Hong Kong23, October 17–19, 2023.



*Correspondence:

AE: alvaro.escudero.saiz@upm.es

Peer review:

Single blind

Copyright:

© 2024 Escudero et al. © This is an open access article distributed under the Creative Commons Attribution Non Commercial No Derivatives License (CC BY-NC-ND 4.0).

Unrestricted use, distribution, and reproduction of the original work are permitted for noncommercial purposes only, provided it is properly cited and its authors credited. No derivative of this work may be distributed.

Keywords:

flutter; vibration amplitude; unsteady pressure; low-pressure turbine; micro-slip; mach number

Citation:

Escudero A., Corral R., and Blando Y. (2024). Mach number influence on low-pressure turbine flutter. *Journal of the Global Power and Propulsion Society*, 8: 62–72.
<https://doi.org/10.33737/jgpps/182890>

Alvaro Escudero^{1*}, Roque Corral¹, Yago Blando¹

¹*School of Aeronautics and Space, Universidad Politécnica de Madrid, 28040 Madrid, Spain*

Abstract

The effect of the Mach number on the vibration amplitude trends of an isolated low-pressure turbine rotor is described. The study utilizes an analytical model correlating the aerodynamic work and the dry-friction work. Aerodynamic damping has been obtained using a frequency domain linearized Navier-Stokes solver, whereas friction damping has been modeled using a heuristic micro-slip model calibrated with the experimental data. In order to validate the analytical predictions, an extensive experimental campaign was conducted. Unsteady pressure transducers flushed mounted in the outer casing, one chord downstream of the trailing edge of the rotor, were used to characterize the vibration of the rotor. The analysis reveals a significant influence of the Mach number on the work balance between aerodynamic and mechanical components. It is observed that the vibration amplitude and the flutter-induced unsteady pressure perturbations of low-pressure turbine rotor blades notably increases when the exit Mach number does.

Introduction

Flutter experiments have been conducted traditionally in sector or annular cascades in academic laboratories prescribing the harmonic motion of a single (Vogt and Fransson, 2006) or a set of airfoils (Bölcs and Fransson, 1986). The unsteady pressures on the airfoil and the aerodynamic work are the output of these experiments. Therefore, they can be regarded as purely aerodynamic experiments for the validation of aerodynamic codes (Fransson and Verdon, 1992). However, cascade testing suffers from several limitations. In the first place, sidewalls contaminate the signal in the instrumented blades (Corral and Gisbert, 2003), especially at high-speed, making the data difficult to use for code validation unless the whole cascade is modelled. Secondly, leakage in the hub is difficult to avoid due to the clearance needed to vibrate the airfoil. Additionally, leakage is difficult to measure and predict. Aside from the intrinsic experimental difficulties, this type of experiment lacks truly aeroelastic dynamics since the free interaction between the fluid and the structure is prevented.

Though many compressor and turbine forced response tests in a controlled environment can be found in the literature, dedicated flutter experiments are scarce because of the difficulty in predicting the final vibration amplitude of the test or its control. Groth et al. (2009) triggered flutter intentionally in a 1.5-stage supersonic turbine blisk and successfully matched the results with CFD predictions. Miura and Sakai (2019) could measure flutter in a rotating labyrinth seal in a dedicated test.

However, the solely dedicated turbine flutter experiment the authors are aware of is that performed by [Corral et al. \(2019\)](#) within the context of the European project FUTURE. An aerodynamically unstable rotor blade was designed to have a wide range of unstable operating points where flutter appears at several nodal diameters. Subsequently, it was tested, and the vibration amplitudes were measured using BTT. Additionally, the unsteady pressures due to blade vibration were recorded using flushed mounted unsteady pressure transducers. Moreover, the rotor was intentionally mistuned to control the rotor blade vibration amplitude. Very recently, a second testing campaign was conducted on a slightly different bladed-disk ([Gallardo et al., 2022](#)) where the number of blades and the tip shroud underwent minor modifications. The main objective of this second campaign was to investigate the effect of superimposing flutter and forced response and include under-platform dampers. Some tests performed in ([Corral et al., 2019](#)) for the baseline configuration without intentional mistuning were repeated in ([Gallardo et al., 2022](#)) with enhanced post-processing techniques. These are the results that are discussed thoroughly in this work.

Unsteady pressure transducers help study turbomachinery flutter because they can provide detailed information about the unsteady pressure fluctuations that occur on the surface of the blades or other components. By measuring unsteady pressure fluctuations, the frequency, nodal diameter, and amplitude of the rotor blade vibration components associated with flutter can be determined.

Turbomachinery is usually designed to be flutter-free. However, it has been shown that cantilever unstable LPT rotor blades can sustain Limit Cycle Oscillations (LCO) induced by flutter and saturated by dry friction in the attachment ([Corral and Gallardo, 2006, 2008](#)). The vibration amplitude of the airfoils is small enough to consider linear aerodynamics ([Corral and Gallardo, 2014](#)), but friction is dominated by micro-slip in the attachment, which is intrinsically nonlinear. Under these circumstances, the problem is not the determination of the stability threshold of the rotor anymore but its vibration amplitude, which is a problem that is far more complicated.

This work describes and discusses the influence of Mach number on low-pressure turbine blade flutter, analysing its impact on the vibration amplitude. The paper is organized as follows. First, the analytical relations between the Mach number, vibration amplitude, and unsteady pressure are introduced. Secondly, the experimental campaign is described briefly. Then the main experimental results are presented. Finally, the experimental results are compared with the predictions of the analytical relations. It is concluded that the Mach number strongly influences the energy balance between aerodynamic damping and friction damping, and that the vibration amplitude of LPT rotor blades increases with the Mach number.

Analysis methodology

Unstable LPT rotors can sustain limit cycle oscillations indefinitely if the vibration amplitude is low enough ([Corral and Gallardo, 2006, 2008](#); [Corral et al., 2019](#)). In the final equilibrium state, the aerodynamic work-per-cycle of the airfoil, W_a , and the dry friction in the blade attachment, W_m , balance, and hence

$$W_a = W_m \quad (1)$$

The unsteady aerodynamics due to the vibration of the airfoil is linear. Hence the aerodynamic work scales with the square of the vibration amplitude of the airfoil, δ_a , i.e. $W_a = W'_a \delta_a^2$, whereas the mechanical damping does as $W_m = W'_m \delta^{*n}$, where δ^* is the displacement in the disk attachment. The exponent n lies in the range $2 \leq n \leq 3$ ([Corral and Gallardo, 2006](#)) and depends on the micro-slip displacement at the fir-tree of the blade and the manner in which the contact is modeled [see the Midlin's model ([Midlin and Deresiewicz, 1953](#)) or the Sellgren and Olofsson model ([Sellgren and Olofsson, 1999](#))]. When the vibration amplitude of the blade is sufficiently small then $n = 3$. If it is assumed that the relationship between the displacement in the fir-tree attachment and the airfoil displacement is linear, i.e. $\delta^* = \beta \delta_a$, then the vibration amplitude is

$$\delta_a^{n-2} = \beta^{-n} (W'_a / W'_m) \quad (2)$$

and the problem consists of determining the expressions of coefficients W'_a and W'_m , the exponent n , and the constant β .

Aerodynamic work estimate

The aerodynamic damping of LPT airfoils can be reproduced using linearised aerodynamic models ([Panovsky and Kielb, 2000](#)). The aerodynamic damping in the present work has been computed using a well-validated

linearised Navier-Stokes solver known as $Mu^2s^2T - L$ (Corral et al., 2003). The main hypothesis is that the flow can be decomposed into a mean flow, which is computed by a steady nonlinear RANS solver (Burgos et al., 2011; Corral et al., 2017) plus an unsteady periodic perturbation, which is Fourier transformed in time and solved using a linearised frequency-domain Navier-Stokes solver.

The aerodynamic work at low-reduced frequencies (Corral and Vega, 2016a,b; Vega and Corral, 2016), such as those present in LPT flutter, can be expressed as

$$W_a = \frac{1}{2} \rho_a U_e^2 S c^{-1} \delta_a^2 \tilde{W}_a(k, \text{IBPA}, C_L, M) = W'_a \delta_a^2 \quad (3)$$

where ρ_a is the air density at the rotor exit, U_e is the exit velocity, S is the rotor surface area, c is the chord of the blade and δ_a is the vibration amplitude of the rotor. The sub-index a is added to remark that this is the characteristic macroscopic displacement of the airfoil, which should not be confused with the displacement in the rotor fir-tree attachment δ .

The dimensionless aerodynamic work-per-cycle \tilde{W}_a depends on the reduced frequency $k = \omega c / U_e$, the Inter-Blade Phase Angle, IBPA, and the airfoil loading, which is represented by the lift coefficient, C_L . Other parameters, such as the Reynolds or Mach numbers, play a minor role. The actual dependence of the minimum aerodynamic damping $W_a^{\min} = \min \tilde{W}_a(\text{IBPA})$ with k is linear at low reduced frequencies (Corral and Vega, 2016a; Vega and Corral, 2016). Flutter severity increases with the loading form but in a more indirect way than with the C_L [see (Corral and Vega, 2017)]. The main impact of the Mach number is frequently related to an increase in the dynamic pressure (i.e. $U_e \propto M_e$) but its influence in dimensionless terms is small. However, the impact of the Mach number on the pressure coefficient distribution along the blade and the lift coefficient, $C_L(M_e)$, gives rise to a slight change in the dimensionless aerodynamic work [see (Vega and Corral, 2017)].

Therefore, the minimum aerodynamic damping and the exit Mach number are related as

$$\frac{W_a^{\min}}{(1/2)\gamma P_0 S c^{-1} \delta_a^2} = \mathcal{F}(M_e) \tilde{W}_a[k(M_e), C_L(M_e)] \text{ where } \mathcal{F}(M_e) = \frac{M_e^2}{(1 + (1/2)(\gamma - 1)M_e^2)^{\gamma/(\gamma-1)}} \quad (4)$$

though it must be stressed that, technically speaking, the sole true dependence on the Mach number, i.e. compressibility, is through the C_L and ρ_a .

Mechanical work estimate

An accurate estimate of the mechanical damping is paramount to determining the rotor blade vibration amplitude and the measured unsteady pressure. Material damping is much smaller than the dry friction in the rotor blade attachment, and can be disregarded safely in the modelling. Dry friction is a nonlinear mechanism responsible for the vibration amplitude saturation in unstable rotor blades (Corral and Gallardo, 2014). In this work, a heuristic approach used previously to predict the vibration amplitude of realistic rotor blades (Corral and Gallardo, 2006, 2008) will be employed to predict firstly the final saturated vibration amplitude of an aerodynamically unstable rotor and then the unsteady pressure perturbations generated due to the vibration. The primary hypothesis is that the normal stresses in the fir-tree contact area due to the pull load are very high. Therefore, the relative displacement between the rotor blade and the disk attachment is small.

Sellgren and Olofsson's micro-slip model (Sellgren and Olofsson, 1999) assumes the contact surface has asperities and a certain roughness. The model relates the tensional state in the contact with the macroscopic displacement using laws different from Coulomb's. The model describes analytically the hysteresis curves of the tangential force in the contact, F , during the preloading as

$$F = \mu N [1 - (1 - \tilde{\delta}^*)^{5/2}] \quad (5)$$

where the dimensionless displacement in the attachment is $\tilde{\delta}^* = \delta^* / \delta_c$, and $\delta_c = \mu E' \lambda / 4G'$ is the characteristic length of the micro-slip, μ is the friction coefficient, N is the normal load, E' and G' are the composite elasticity and shear modulus respectively, and λ the contact penetration length. It may be shown that, if the hysteresis loop is symmetric, i.e.: $F^* = F_U = F_L$ and $\delta^* = y_U = y_L$, the work per cycle is

$$\frac{W_m}{\mu N \delta_c} = 4(2 - \tilde{F}^*) \tilde{\delta}^* + \frac{16}{7} [(1 - \tilde{\delta}^*)^{7/2} - 1] \quad (6)$$

where $\tilde{F}^* = F^*/\mu N = 1 - (1 - \tilde{\delta}^*)^{5/2}$ is the dimensionless tangential force. If $\tilde{\delta}^* \ll 1$, or in other words, if the tangential force $F \ll \mu N$ then it may be shown that

$$\tilde{W}_m = \frac{W_m}{\mu N \delta_c} \simeq \frac{15}{6} \tilde{\delta}^{*3} \quad (7)$$

The scaling of the mechanical work with an exponent greater than two is essential for the stabilization of aerodynamically unstable rotors.

Estimate of the vibration amplitude

The vibration amplitudes that appear in the aerodynamic damping, δ_a , [see Equation (3)], and the mechanical work, δ^* , [see Equation (6)] are not only different but have different orders of magnitude. While the former relates to the macroscopic rotor blade displacement, the latter, $\delta_{FT} = \delta^*$, relates to the relative displacement between the rotor blade and the disk in the fir-tree attachment. An approximate relationship between both to close the problem was provided in (Corral and Gallardo, 2006, 2008), but it is summarised here for completeness.

Since the magnitude of the displacements in the fir-tree and rotor blade tip are very different, it is convenient to express the mechanical work as a function of the alternate tangential force in the attachment, \tilde{F}^* , since it is easier to link with the macroscopic displacement. If $\tilde{\delta}^* \ll 1$ then Equation (6) reduces to $\tilde{F}^* = (5/2)\tilde{\delta}^*$, and Equation (7) becomes

$$\tilde{W}_m = \frac{W_m}{\mu N \delta_c} \simeq \frac{4}{25} \tilde{F}^{*3} \quad (8)$$

However, if $\tilde{\delta}^* \sim \mathcal{O}(1)$, Equation 5 must be injected into Equation (6) to obtain $\tilde{W}_m = \tilde{W}_m(\tilde{F}^*)$.

The next step is to relate the alternate tangential force or stress at the attachment to the blade vibration. If the rotor blade is modelled as beam clamped in the attachment then the alternate moment, M is

$$M_b = EI_{y_{zz}} \simeq m_a L \omega_n^2 \delta_a Y_{\xi\xi}(0) \quad (9)$$

where m_a is the rotor blade mass, L the height of the blade including the shank, and ω_n the natural frequency of the blade. $Y_{\xi\xi}(0)$ is a constant that depends on the beam boundary conditions at the attachment. This relation can be obtained too from a FEM. If the internal dynamics of the attachment is neglected (Corral and Gallardo, 2006) then this momentum has to be balanced by the vertical alternate reaction in the fir-tree. It can be shown that

$$\tau = \frac{F}{A_c} \propto \frac{m_a L \omega_n^2 \sin \alpha}{A_c a_{FT} m_{\text{lob}}} \delta_a \quad (10)$$

where a_{FT} is the half-width of the fir-tree, α the inclination angle of the contact surface, A_c , and m_{lob} the number of lobes. The above expression allows to close the model except from a constant that is derived from experimental data (Corral and Gallardo, 2006).

Estimate of the unsteady pressure component due to flutter

In this work, flutter severity is measured using unsteady pressure transducers. It is, therefore, paramount to estimate the component of the unsteady pressure associated with flutter. In the low-reduced frequency limit, i.e. $k \ll 1$, the characteristic unsteady pressure on the airfoil can be estimated as $p'_c \propto \rho_e U_e^2 (\delta_a/c)$. It has been shown that the vibration amplitude $\delta_a^{n-2} \propto W'_a/W'_m$, where $n = 2.5$ or 3 depending on whether the vibration amplitude in the attachment is small or large respectively. The component associated with the dry friction, W'_m depends mainly on geometric factors, the natural frequency of the blade, and the shaft speed. For a given rotor blade and shaft speed, W'_m is constant and hence $\delta_a^{n-2} \propto W'_a$. The blade vibration amplitude scales [using Equation (4)], as $\delta_a^{n-2} \propto \mathcal{F}(M_e^2)$. Finally, if \tilde{W}_a is deemed approximately constant in the Mach number range of

interest, the unsteady pressure scales approximately

$$p'_c \propto (\mathcal{F}(M_e^2))^{(n-1)/(n-2)} \quad (11)$$

The main conclusion is that the sensitivity of the unsteady pressure due to the exit Mach number is very high.

Experimental results

Wind-tunnel and rig description

An isolated shrouded high aspect ratio LPT rotor blade was tested in the CTA high-speed wind tunnel during 2022 (Gallardo et al., 2022). The rotor blade used in this second experimental campaign is similar to that described in Corral et al. (2019) and tested in 2011. The aerodynamic shape and the two-lobe fir-tree attachment with the disk used in both experimental campaigns are the same, but the blade count was reduced from 146 to 144 to ease the grouping of blades in packets. The tip-shroud of the rotor blade was designed to accommodate a rear magnet to excite the rotor in a separate in-vacuum test to characterise the damping of the bladed-disk. The two rotor blades are very similar from a dynamic point of view. A more thorough description of the test can be found in Corral et al. (2019) and Gallardo et al. (2022).

The experiment uses an isolated bladed rotor subject to the incoming conditions of the facility VIGVs, which are located more than ten chords upstream of the testing article. Therefore, the rotor blade is considered isolated and subject only to the weak perturbations associated with the blade-passing frequency of the upstream VIGVs, whose chord is about 50% longer than that of the rotor blade. The boundary layer generated at the inlet duct is sucked one chord upstream of the rotor to avoid unrealistic effects in the secondary flow vortex system. A general layout of the wind tunnel can be seen in Figure 1(left).

The instrumentation used to measure aerodynamics includes total pressure and total temperature rakes located at the inlet and outlet of the rotor. Inlet and outlet boundary conditions of the row were acquired using fast-response five-hole miniaturized probes that are radially and azimuthally traversed across a distance equivalent to several rotor pitches. Blade Tip-Timing (BTT) optical probes were installed in the outer casing, pointing radially to the rotor to measure the vibration amplitude of every individual blade. Finally, unsteady pressure transducers (Kulite XT-190M) were flush-mounted in the outer casing, one chord downstream of the rotor blade.

Unsteady pressure measurements

Unsteady pressure transducers are flush mounted in the outer casing, one chord downstream of the trailing edge of the rotor blade. Each pressure transducer records the unsteady pressure signal for 40 seconds with a sampling frequency of 25.6 kHz, which is much higher than the range of interest, that in this case, oscillates between 500 and 2,000 Hz. Pressure signals are segmented into one-second windows, Fourier transforms in time are performed on each window, and their Fourier coefficients are time-averaged. Afterward, Fourier transforms of

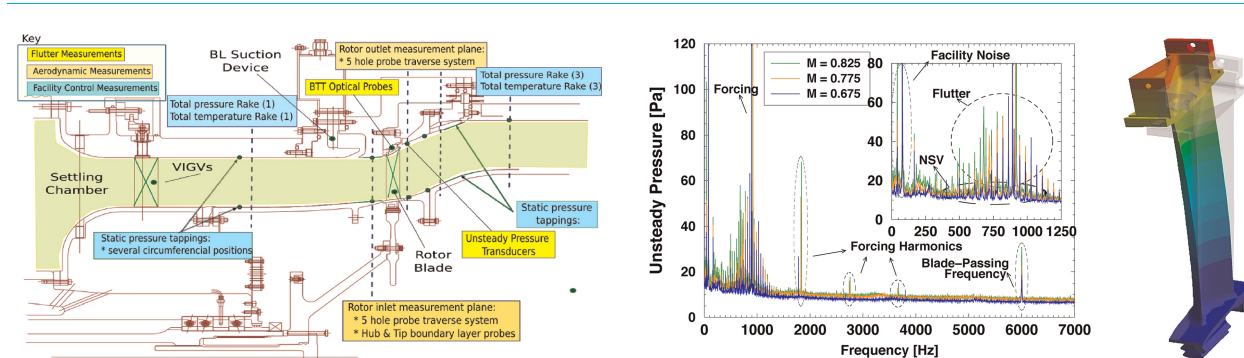


Figure 1. Layout of the CTA wind-tunnel used for the experimental campaign (left), time and circumferential averaged Fourier transform of the unsteady pressure signals obtained for $\Omega = 103\%$, $\rho = 100\%$ and three different levels of exit Mach number ($M_e = 0.675$, $M_e = 0.775$ and $M_e = 0.825$) (center) and modeshape of the first flap mode (right).

different pressure transducers located at different circumferential positions are averaged to obtain the mean representation of the signal's harmonic content.

The test matrix of the experimental campaign includes different intentional mistuning patterns, forcing mechanisms (using magnets on the tip-shroud of the blade), a wide range of rotational speeds, densities and three levels of exit Mach number. However, the present study has been carried out for the baseline configuration without magnets and without intentional mistuning patterns. Three different exit Mach numbers at different rotational speeds have been analyzed. [Figure 1](#)(center) shows the harmonic content of the unsteady pressure transducers for $\Omega = 90\%$, the baseline level of density ($\rho = 100\%$), and three different exit Mach numbers ($M_e = 0.675, 0.775$ and 0.825).

The acoustic responses can be divided into different families depending on the source of the excitation. [Figure 1](#)(center) shows five families of peaks sorted from low to high frequency corresponding to facility noise, non-synchronous vibration whose source has not been identified, together with a strong forcing and its harmonics, flutter signals as a result of the blade vibration due to different unstable nodal diameters, and the blade-passing frequency.

Since the present paper aims to study the evolution of flutter peaks with the exit Mach number, the frequency range shown below is limited to the frequencies of interest for flutter, coinciding with the Doppler-shifted frequency of the unstable nodal diameters. Then, the vibration frequency in the stationary frame of reference is

$$\omega = \omega_n + ND \cdot \Omega \quad (12)$$

in physical terms, the frequency separation between different flutter peaks is Ω . One of the main advantages of unsteady pressure sensors over BTT measurements is that they can easily identify the unstable NDs of the flutter signals by their associated Doppler-shifted frequency.

Rotor blade design

Aerodynamic design

The rotor blade aerodynamic design is representative of an aeronautical low-speed LPT. The total deflection is about 100 deg, the lift coefficient of the blade sections is around 1, and the exit Mach number is high subsonic. In particular, the design intent of the 70% span section is given in [Table 1](#), for more information, the interested reader is referred to [Corral et al. \(2019\)](#) and [Gallardo et al. \(2022\)](#).

[Figure 2](#)(left) displays the isentropic Mach number, M_{is} , of the 70% section and 90% of the nominal shaft speed, Ω , for three different pressure ratios. The section is located out of the secondary flow region. The airfoil operates at a slight positive incidence at these speeds, inducing a front-loaded distribution. At high Mach numbers ($M_e = 0.775$ and 0.825), the M_{is} and C_p distributions exhibit an overshoot on the suction side since the rotor blade was designed for a lower Mach number ($M_e \simeq 0.7$). Another interesting and well-known behaviour is that the front loading of the blade is reduced when the Mach number is increased [see [Figure 2](#)(right)].

Aeroelastic design

The tested bladed disk consists of a disk stiff enough to ensure a small participation of the disk, except perhaps in the first four NDs. [Figure 1](#)(right) shows the first mode of the blade, which is a flap mode. It is well-separated in frequency for all the ND from the second mode to avoid interactions among them. The natural frequency of the first mode is about 186 Hz at design conditions, increasing slightly with the rotational speed.

The reduced frequencies of the first mode, $k = \omega c / U_e$, based on the axial chord and exit velocity of the 70% section, at $\Omega = 90\%$ are $k = 0.112, 0.105$ and 0.092 for $M_e = 0.675, 0.775$ and 0.825 , respectively. The slight

Table 1. Boundary conditions for the design intent of the 70% span rotor blade section.

M_{in}	α_{in}	M_{exit}	α_{exit}	Re
0.42	36.5°	0.75	60°	1.2×10^5

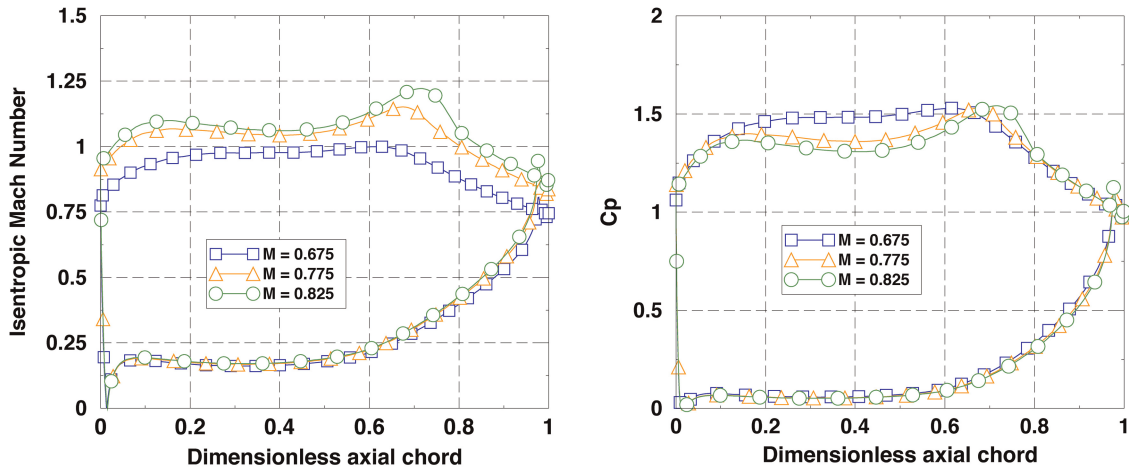


Figure 2. Isentropic Mach number (left) and pressure coefficient (right) distribution at 70% height and $\Omega = 90\%$.

decrease in the reduced frequency is mainly associated with the increase in the exit velocity. The critical damping ratio, ξ , and the dimensionless aerodynamic damping are related by:

$$\xi = \frac{\mu \tilde{W}_a}{k} \tag{13}$$

where $\mu = \rho_a S/m$ is the mass ratio, and m is the modal mass. The impact of the increase of k in the critical damping ratio with the Mach number, through $\tilde{W}_a[k(M_e), C_L(M_e)]$ is negligible since the variation in k is about 20% in the range of interest, and the C_L or Swiffel numbers are $C_L = 1.195, 1.182$ and 1.180 for $M_e = 0.675, 0.775$ and 0.825 , respectively.

The critical damping ratio, ξ , of the first mode for $\Omega = 90\%$, computed using a linearized frequency domain solver (Corral et al., 2003), is displayed in Figure 3(left). It can be seen that the flap mode exhibits several highly unstable nodal diameters. This situation is frequently seen in aeronautical cantilever LPT rotor blades and the values of k and ξ fully representative of an aeronautical LPT rotor blade (Corral and Gallardo, 2014). The change of the aerodynamic damping with the incidence (shaft speed) is moderate (not shown here for the sake of brevity), whilst ξ is proportional to the facility density level, as it was shown in Corral et al. (2019).

Figure 3(right) displays the critical damping ratio ξ scaled with the inverse of the Mach number function, $\mathcal{F}(M_e^2)$, given in Equation (4), as a function of the ND for different Mach numbers. It can be seen that despite the change in the steady blade loading due to the Mach number [Figure 2(right)] and the change in the reduced frequency, the three damping curves collapse into a single one. A similar behaviour was reported by Corral and Vega (2016b) but with a simpler M_e^2 scaling on the aerodynamic influence coefficients. The matching between

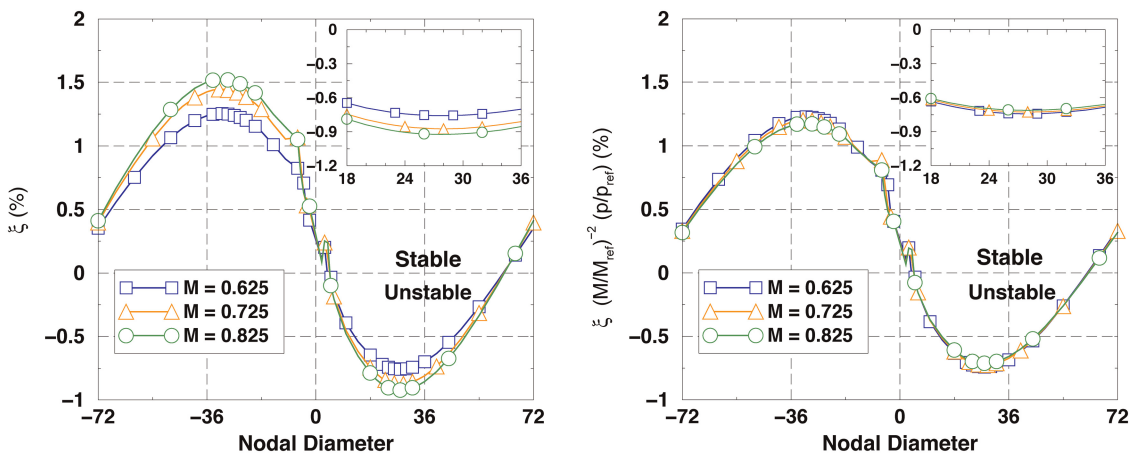


Figure 3. CDR and CDR scaled with the exit static pressure and the inverse of M_e^2 normalised with the factor for $M_{ref} = 0.625$ for $\Omega = 90\%$ ($N = 2,500$ rpm).

the three curves is remarkable validating the expression 4 to scale the aerodynamic damping for different pressure ratios.

Analysis of experimental results

Figure 4 shows the harmonic content of the flush-mounted unsteady pressure transducers for different shaft speeds and exit Mach numbers as a function of the ND. Only the NDs associated with flutter signals identified using a bladed-disk FE model are shown. All the peaks that do not correspond to a fluttering ND have been filtered out for the sake of clarity. The highest peak corresponds to the most unstable ND, which can be found in Figure 3 and is around $ND = 26$. Nevertheless, aerodynamic damping analyses did not take mistuning into account.

Several studies (Crawley and Hall, 1985; Kielb and Kaza, 1984; Martel et al., 2008) show that the effect of mistuning on flutter is beneficial since it tends to reduce the overall aeroelastic instability of the rotor. It has been shown analytically that the final state of a bladed disk with multiple unstable NDs contains only the most unstable ND (Corral and Gallardo, 2014). Natural mistuning is present in the tested bladed disk, and the measurements obtained in a ping test were reported in (Corral et al., 2019). The importance of mistuning is relative to the effect of aerodynamic forces, so if the dynamic head or the Mach number increase, the response of the system resembles more that of a tuned bladed-disk. Mistuning gives rise to sidebands of decreasing amplitude around the most unstable ND in the response, as shown in Figure 4. The sideband bands corresponding to the less unstable NDs are hardly distinguished since their amplitudes are very small and not detectable by the unsteady pressure transducers.

The experimental results show a variation of the most unstable ND with the exit Mach number changes, whereas the numerical predictions of the tuned aerodynamic damping indicate that the most unstable ND remains unaffected by the Mach number. This discrepancy is attributed to the presence of mistuning, an effect that has not considered in the numerical predictions. Therefore, the highest unsteady peak denotes that the blade is vibrating the highest in that particular ND, which changes with the exit Mach number due to natural mistuning. All the pressure perturbations induced by flutter are cut-off and their decay rate change from ND to ND, but the distance from the trailing edge of the rotor to the transducer is small; hence, the impact on the measured pressure amplitude is deemed small too.

Comparison of analytical and experimental results

The analytical results obtained with the model are compared to the experimental results in this section. Figure 5 shows the mean unsteady pressure as a function of the exit Mach number for different shaft speeds. The mean unsteady pressure is computed by subtracting the background noise from the 15 highest peaks and averaging them. The analytical trend is calibrated with the data at the highest available Mach number at each rotational speed. The Mach number at which the calibration is performed is appropriately labeled for each case.

The dashed line in Figure 5 is computed using Equation (11) using $n = 2.5$. It can be seen that the unsteady pressure peaks around $\Omega = 103\%$; this is consistent with BTT data measured in the current experimental campaign and the results reported in Corral et al. (2019). The prediction of the unsteady pressure trend by the model is correct in overall, except for the case at $\Omega = 90\%$ and $M_e = 0.675$, which is an outlier that is not fully understood. It is concluded that the underlying reason for the good prediction of the model is that this retains the physics of the problem.

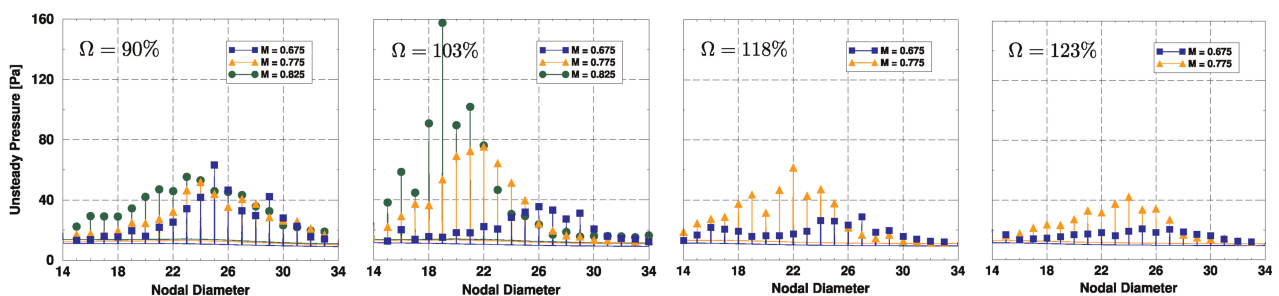


Figure 4. Time and circumferential averaged Fourier transform of the unsteady pressure signals filtered to show the flutter-induced peaks for different exit Mach numbers.

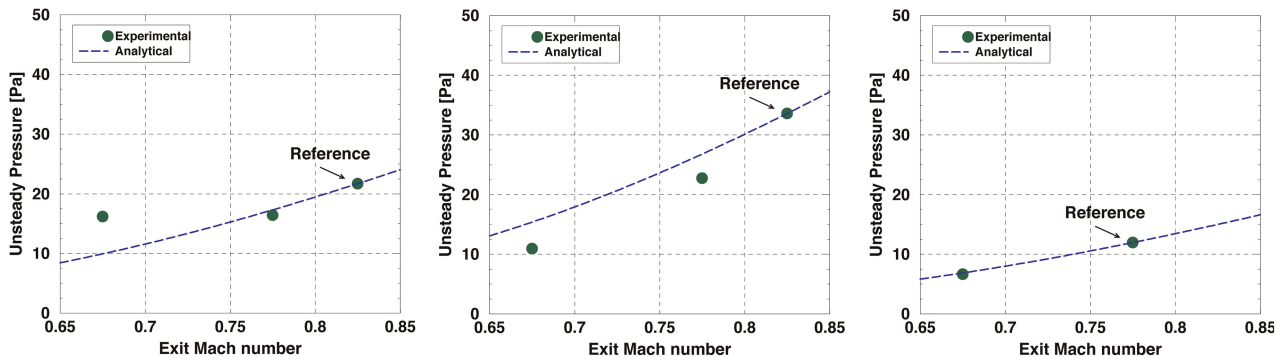


Figure 5. Mean unsteady pressure signal for different shaft speeds and Mach numbers compared to the trends obtained by the analytical model for each of the shaft speeds.

Concluding remarks

The unsteady pressure transducer data of a low-pressure turbine rotating rig have been post-processed to isolate the signals associated with flutter-induced vibration. The study is focused on the impact of the Mach number on the flutter severity though results are presented for several shaft speeds. The vibration amplitude variation with the shaft speed is involved and is not discussed in this work.

The aerodynamic damping characteristics of the rotor blade have been computed using a linearised Navier-Stokes solver. It is shown that a proper non-dimensionalization can absorb the impact of the Mach number on the critical damping ratio and that this scales as $\xi \propto M^2 / (1 + \frac{\gamma-1}{2} M^2)^{\gamma/(\gamma-1)}$.

The mechanical work is estimated using a simplified micro-slip model linked to an aerodynamic model to predict the rotor blade vibration amplitude. The vibration amplitude is then translated into unsteady pressure and compared to the experimental data. The exit Mach number was varied between 0.6 and 0.8, and within this range, significant variations on the unsteady pressure (and vibration amplitude) were found. The model predicted the unsteady pressure's dependence on the Mach number.

Nomenclature

a_e	Speed of sound at the exit
BTT	Blade Tip Timing
c	Airfoil chord
CDR	Critical Damping Ratio
CTA	Centro de Tecnologías Aeronáuticas
E', G'	Elasticity and shear modules
k	$= \omega c / U_e$, Reduced frequency
IBPA	Inter-Blade Phase Angle
LPT	Low-Pressure Turbine
m	Modal mass
M	Mach number
M_b	Blade alternate moment
ND	Nodal diameter
p_e	Exit static pressure
P_0	Inlet total pressure
S	Airfoil surface
U_e	Exit velocity
W_{cyc}	Work per cycle
Re	Reynolds number

Greek symbols

β	$= \delta^* / \delta_a$, fir-tree attachment and airfoil displacement ratio
γ	Heat capacity ratio

- δ^* Fir-tree vibration amplitude
 δ_a Airfoil vibration amplitude
 $\delta_c = \mu E' \lambda / 4G'$, characteristic value of fir-tree displacements
 μ Friction coefficient or mass ratio
 λ Penetration length in the contact
 ρ_a Density of air
 ω Vibration angular frequency (rad/s)
 ξ Critical Damping ratio (%)
 Ω Shaft speed (%)

Super-scripts

- \sim Non-dimensional values

Sub-scripts

- e Exit

Acknowledgments

The authors want to thank all the participants of the ARIAS work package two for their contribution to setting up the CTA experimental campaign and the rotor blade redesign. The authors want to thank ITP for providing access to ITP's design system.

Funding sources

This work has been partially funded by the ARIAS ("Advanced Research Into Aeromechanical Solutions") project, funded by the European Union's Horizon 2020 research and innovation programme under grant agreement No.769346. This work has been also partially funded by the TASTE project under grant agreement No. RTC2019-007194-4.

Competing interests

Alvaro Escudero declares that he has no conflict of interest. Roque Corral declares that he has no conflict of interest. Yago Blando declares that he has no conflict of interest.

References

- Bölcs A. and Fransson T. H. (1986). Aeroelasticity in turbomachines: Comparison of theoretical and experimental cascade results. In Tech. Rep., Laboratoire de Thermique Appliquee et de Turbomachines. EPFL.
- Burgos M., Corral R., and Contreras J. (2011). Efficient edge based rotor/stator interaction method. *AIAA Journal*. 41 (1): 19–31. <https://doi.org/doi.org/10.2514/1.44512>.
- Corral R. and Gisbert F. (2003). A numerical investigation on the influence of lateral boundaries in linear vibrating cascades. *ASME Journal of Turbomachinery* 125 (3): 433–441. <https://doi.org/10.1115/1.1575255>.
- Corral R. and Gallardo J. M. (2006). A methodology for the vibration amplitude prediction of self-excited rotors based on dimensional analysis. In ASME Paper 2006-GT-90668. Vol. 5. Proceedings of the 51st ASME Gas Turbine and Aero engine Congress, Exposition and Users Symposium, Barcelona, Spain. pp. 1101–1113.
- Corral R. and Gallardo J. (2008). Verification of the vibration amplitude prediction of self-excited lpt rotor blades using a fully coupled time-domain non-linear method and experimental data. In: ASME Paper 2008-GT-51416. Vol. 5. Proceedings of the 51st ASME Gas Turbine and Aero engine Congress, Exposition and Users Symposium, Berlin, Germany, pp. 835–847.
- Corral R. and Gallardo J. (2014). Nonlinear dynamics of bladed disks with multiple unstable modes. *AIAA Journal*. 56 (6): 1124–1132. <https://doi.org/10.2514/1.J051812>.
- Corral R. and Vega A. (2016a). The low reduced frequency limit of vibrating airfoils – Part i: Theoretical analysis. *ASME Journal of Turbomachinery* 138 (2): 021004. <https://doi.org/10.1115/1.4031776>.
- Corral R. and Vega A. (2016b). Physics of vibrating turbine airfoils at low reduced frequency. *AIAA Journal of Propulsion and Power*. 32 (2): 325–336. <https://doi.org/10.2514/1.B35572>.
- Corral R. and Vega A. (2017). Quantification of the influence of unsteady aerodynamic loading on the damping characteristics of oscillating airfoils at low reduced frequency. Part I: Theoretical support. *ASME Journal of Turbomachinery* 139 (3): 0310009. <https://doi.org/10.1115/1.4034976>.

- Corral R., Escribano A., Gisbert F., Serrano A., and Vasco C. (2003). Validation of a linear multigrid accelerated unstructured navier-stokes solver for the computation of turbine blades on hybrid grids. In AIAA Paper 2003-3326. 9th AIAA/CEAS Aeroacoustics Conference, Hilton Mead, South Carolina.
- Corral R., Gisbert F., and Pueblas J. (2017). Efficient execution of a parallel edged-based navier-stokes solver on graphics processing units. *International Journal of Computational Fluid Dynamics* 31 (2): 1–16. <https://doi.org/10.1080/10618562.2017.1294686>.
- Corral R., Beloki J., Calza P., and Elliot R. (2019). Flutter generation and control using mistuning in a turbine rotating rig. *AIAA Journal*. 57 (2): 782–795. <https://doi.org/10.2514/1.J056943>.
- Crawley E. F. and Hall K. C. (1985). Optimization and mechanisms of mistuning in cascades. *ASME Journal of Engineering for Gas Turbines and Power* 107 (2): 418–426. <https://doi.org/10.1115/1.3239742>.
- Fransson T. H. and Verdon J. M. (1992). Updated report on standard configurations for unsteady flow. In Tech. Rep., KTH.
- Gallardo J., Oscar B., Hernandez J., Garcia G., Gallego J., et al. (2022). Experimental research into aeroelastic phenomena in turbine rotor blades inside arias eu project. In ISUAAAT 16. No. ISUAAAT16- 30.
- Groth P., Martensson H., and Andersson C. (2009). Design and experimental verification of mistuning of a supersonic turbine blisk. *ASME Journal of Turbomachinery* 132 (1): 011012–011012–9. <https://doi.org/10.1115/1.3072492>.
- Kielb R. and Kaza K. (1984). Effects of structural coupling on mistuned cascade flutter and response. *ASME Journal of Engineering for Gas Turbines and Power* 106 (1): 17–24. <https://doi.org/10.1115/1.3239532>.
- Martel C., Corral R., and Llorens J. M. (2008). Stability increase of aerodynamically unstable rotors using intentional mistuning. *ASME Journal of Turbomachinery* 133: 1–11.
- Midlin R. D., and Deresiewicz H. (1953). Elastic spheres in contact under varying oblique forces. *Journal of Applied Mechanics*. 20: 327–344. <https://doi.org/10.1115/1.4010702>.
- Miura T., and Sakai N. (2019). Numerical and experimental studies of labyrinth seal aeroelastic instability. *ASME Journal of Engineering for Gas Turbines and Power* 141 (11): 111005. <https://doi.org/10.1115/1.4044353>.
- Panovsky J., and Kielb R. (2000). A design method to prevent low pressure turbine blade flutter. *ASME Journal of Engineering for Gas Turbines and Power* 122 (1): 89–98. <https://doi.org/10.1115/1.483180>.
- Sellgren U. and Olofsson U. (1999). Application of a constitutive model for micro-slip in finite element analysis. *Computer Methods in Applied Mechanics and Engineering*. 170 (1): 65–77. [https://doi.org/10.1016/S0045-7825\(98\)00189-3](https://doi.org/10.1016/S0045-7825(98)00189-3).
- Vega A. and Corral R. (2016). The low reduced frequency limit of vibrating airfoils - Part II: Numerical experiments. *ASME Journal of Turbomachinery* 128 (2): 021005. <https://doi.org/10.1115/1.4031777>.
- Vega A. and Corral R. (2017). Quantification of the influence of unsteady aerodynamic loading on the damping characteristics of oscillating airfoils at low reduced frequency. part ii: Numerical verification. *ASME Journal of Turbomachinery* 139 (3): 031010. <https://doi.org/10.1115/1.4034978>.
- Vogt D. and Fransson T. (2006). Experimental investigation of mode shape sensitivity of an oscillating low-pressure turbine cascade at design and off-design conditions. *ASME Journal of Engineering for Gas Turbines and Power* 129 (2): 530–541. <https://doi.org/10.1115/1.2436567>.